Chinese Chemical Letters 35 (2024) 108933

Contents lists available at ScienceDirect

Chinese Chemical Letters

journal homepage: www.elsevier.com/locate/cclet

Dual-functional POM@IL complex modulate hole transport layer properties and interfacial charge dynamics for highly efficient and stable perovskite solar cells

Boyuan Hu, Jian Zhang*, Yulin Yang*, Yayu Dong, Jiaqi Wang, Wei Wang, Kaifeng Lin, Debin Xia

MIIT Key Laboratory of Critical Materials Technology for New Energy Conversion and Storage, School of Chemistry and Chemical Engineering, Harbin Institute of Technology, Harbin 150001, China

ARTICLE INFO

Article history:
Received 30 June 2023
Revised 31 July 2023
Accepted 14 August 2023
Available online 15 August 2023

Keywords:
Polyoxometalates
Ionic liquid
Perovskite solar cells
Energy alignment
Humidity stability

ABSTRACT

The severe interfacial charge recombination as well as the stability issues brought by the Li-TFSI still hinder the commercialization of high-performance perovskite solar cells (PSCs). Here, a polyoxometalates (POMs)-based complex, POM@ ionic liquid (IL), is synthesized and applied as an effective additive that simultaneously enhances the performance and stability of PSCs. The interactions between POM@IL complex and Li-TFSI inhibit the aggregation of Li-TFSI. The synergistic oxidation of POM@IL complex and Li-TFSI towards 2,2′,7,7′-tetrakis[*N*,*N*-di(4-methoxyphenyl)amino]-9,9'-spirobifluorene (Spiro-OMeTAD) effectively enhances the electrical properties of hole transport layer film and the photovoltaic performances of PSCs. The champion device modified with the POM@IL complex yields an excellent power conversion efficiency (PCE) of 22.73%. Moreover, the incorporation of POM@IL improves the humidity stability of PSCs. After storing under high humidity conditions (25 °C, 60% RH) for 1200 h, the POM@IL modified device retained a remarkable 81.2% of its initial PCE. This work provides new insight into constructing POMs-based materials for high-performance photovoltaic devices.

The power conversion efficiency (PCE) of the organic-inorganic hybrid perovskite solar cells (PSCs) has reached up to 25.7% due to the appealing feature of perovskite materials [1,2]. Amongst, the highest PCEs of n-i-p type PSCs are mostly achieved utilizing p-doped 2,2′,7,7′-tetrakis[*N*,*N*-di(4-methoxyphenyl)amino]-9,9′-spirobifluorene (Spiro-OMeTAD) as hole transport layer (HTL) material [3–8]. However, the practical application of PSCs has been hindered by the poor charge transportation/extraction kinetics across the perovskite/HTL interface that originated from the inferior intrinsic conductivity of Spiro-OMeTAD [9–15]. Although Li-TFSI has been proven to be a popular dopant for Spiro-OMeTAD to address the conductivity issues by facilitating the oxidation process of Spiro-OMeTAD in the ambient atmosphere [16–20]. The tendency of Li^+ to absorb water from the air as well as its migration and accumulation in HTL or across the interface seriously degrade the HTL film and affect the interfacial energy alignment, which eventually deteriorates the performances of PSCs [21–26].

Polyoxometalates (POMs) is a class of polyanionic clusters that consists of early transition metals at their highest-oxidation-state (such as Mo^{6+}, V^{5+}, W^{6+}), which granted them revisable oxidation abilities [27–29]. The oxo-linked MO_x polyhedron structures and well-defined units of POMs endow them with excellent thermal and oxidative stabilities [30–32]. Due to their appealing features, POMs have been widely applied in the fields of catalysis, medicine, nanoscience, and photovoltaic conversion [33–35]. By constructing POM-based complexes with POMs and diverse organic molecules (*e.g.*, ionic liquid (IL)), we could further broaden the applications of POMs with electronic versatility and peculiar structures [36,37]. Combining both the chemical properties of POMs anions and organic functional groups, we can design a POM-based complex that perfectly handles the electrical and stability issues faced by PSCs.

Herein, we have designed and synthesized the POM@IL complex based on phosphomolybdic acid and 1-(2-hydrazinyl-2-oxoethyl)pyridin-1-ium chloride through a facile co-precipitate method (Supporting information). We selected the Keggin-type PMo_{12} with excellent oxidation abilities to produce high concentrations of Spiro-OMeTAD$^+$ under an inert condition and improve the electrical properties of HTL. The abundant O functional groups

* Corresponding authors.
E-mail addresses: zhaji@hit.edu.cn (J. Zhang), ylyang@hit.edu.cn (Y. Yang).

https://doi.org/10.1016/j.cclet.2023.108933
1001-8417/

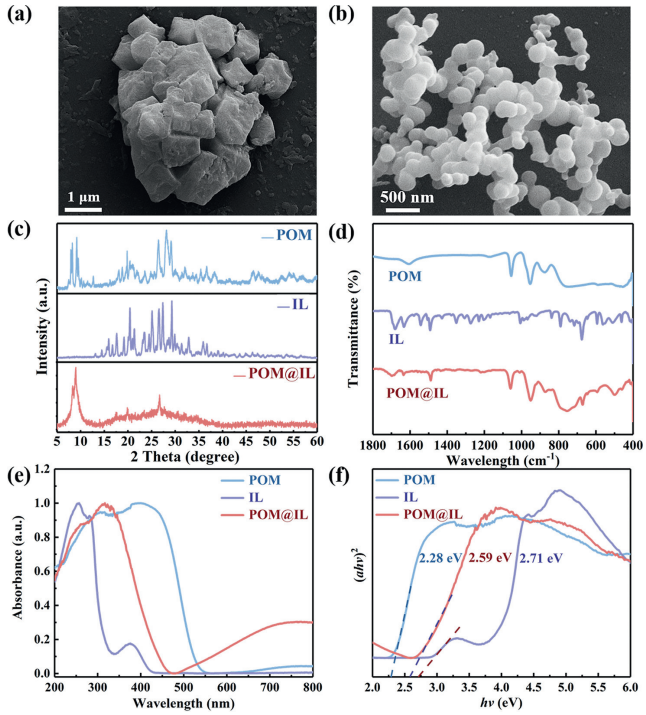

Fig. 1. The SEM images of the (a) POMs cluster and (b) the as-synthesized POM@IL complex. (c) XRD patterns, (d) FT-IR spectra, (e) UV-vis spectra, and (f) tauc plots of POM, IL, and POM@IL complex.

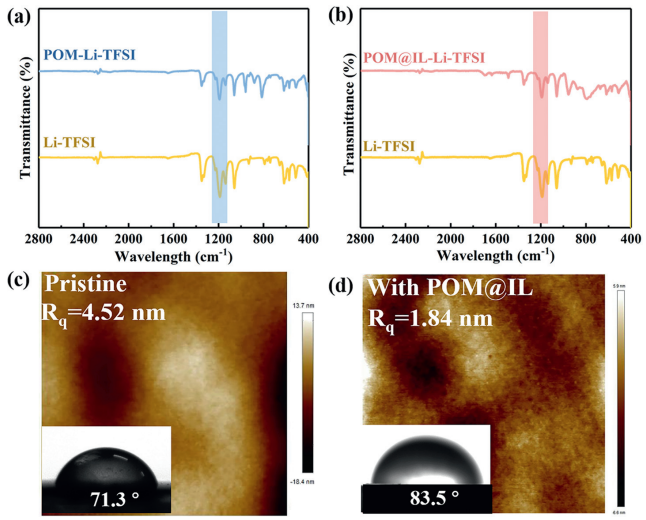

Fig. 2. (a) The FT-IR spectra of POM, Li-TFSI, and the mixture of POM and Li-TFSI. (b) FT-IR spectra of POM@IL, Li-TFSI, and the mixture of POM@IL and Li-TFSI. AFM images and water contact angles based on (c) pristine HTL film and (d) HTL film modified with POM@IL complex.

could provide anchoring sites for Li^+ and stabilize the Li-TFSI. Ionic liquid, 1-(2-hydrazinyl-2-oxoethyl)pyridin-1-ium chloride, was selected to electrostatically interact with POMs to enhance the hydrophobicity, the hydrazine and carbonyl functional groups helped to passivate the interfacial defects and further decrease the interfacial recombination losses.

Scanning electron microscope (SEM) images in Figs. 1a and b showed that the POM@IL complex possesses a regular grain size of around 200–300 nm, whereas the pristine POMs cluster exhibited a grain size of around 1 μm and tended to agglomerate. The interactions between POMs and IL could effectively reduce the grain size as well as avoid agglomeration. X-ray diffraction (XRD) patterns of POM, IL, and POM@IL complex in Fig. 1c disclosed that only the characteristic peaks corresponding to the Keggin structure in the range of 5°–10° and partial of the characteristic peaks that related to the IL were preserved in the POM@IL complex. The POMs cluster turned from a crystalline phase towards an amorphous phase after being electrostatically attracted to IL [38]. As is shown in the Fourier transform infrared (FT-IR) spectra of POM, IL, and POM@IL in Fig. 1d. The shifts of the vibration peaks around 838, 1007, 1230, and 1274 cm^{-1} that attributed to the pyridine group, as well as the shifts of the characteristic peaks around 770, 878, 953 and 1056 cm^{-1} that attributed to the Mo-O_c-Mo, Mo-O_b-Mo, Mo=O_d and P-O_a, verified the interactions between POM and IL. These phenomena are closely related to the changes in electron clouds around the binding sites. It can be seen in the UV-vis absorption spectra in Fig. 1e that compared with the POMs cluster, the POM@IL complex exhibited decreased optical absorption around 350–550 nm, which verified the orbital change of the POM@IL complex. The optical bandgap (E_g) of the POM@IL complex was increased from 2.28 eV (POM cluster) to 2.59 eV (Fig. 1f).

We have mixed POM, IL, and POM@IL complex with Li-TFSI in acetonitrile, respectively, to investigate the interactions between Li^+ and O functional groups. As shown in Figs. 2a and b, the characteristic peaks around 1186 and 1059 cm^{-1} were attributed to the O=S=O symmetric and antisymmetric stretching, respectively. After mixing with the POMs cluster, the O=S=O symmetric peaks around 1186 cm^{-1} shifted towards 1191 cm^{-1} [39], which confirmed the successful anchoring of Li-TFSI on the rich O function groups. When mixing Li-TFSI with IL, the O=S=O symmetric peaks in Li-TFSI didn't show shifts (Fig. S1 in Supporting information), which indicates that there were no electrostatic or covalent interactions between IL and Li-TFSI. Moreover, we speculate that the positively charged IL would act as a repelling agent that generates electrostatic repulsion with Li-TFSI. As the electrostatic attractions between the POMs cluster and IL gathered more electrons around binding sites and changed the electron clouds, we speculate that the POM@IL complex possesses a higher affinity towards Li^+, thus providing more powerful anchoring sites for Li-TFSI. The more significant shift of characteristic O=S=O symmetric peak from 1186 cm^{-1} towards 1193 cm^{-1} for the mixture of POM@IL and Li-TFSI further validated our speculation. Moreover, after the addition of POM and POM@IL complex, the F 1s signals corresponded to the $TFSI^-$ and Li-F (Fig. S2 in Supporting information) were observed to shift towards lower binding energies. The more evident shift of F 1s spectra indicated a more powerful affinity between the POM@IL complex and Li-TFSI.

The effective stabilization of Li-TFSI and the avoidance of aggregation would facilitate a pinhole-free morphology of HTL film as well as promote favorable morphological contact with perovskite, moreover, the hydrophobicity of HTL film would be enhanced. We have performed atomic force microscopy (AFM) images and water contact angles based on pristine HTL films and HTL films modified with POMs, IL and POM@IL, respectively (Figs. 2c and d, Fig. S3 in Supporting information). As can be seen, the POM@IL complex-modified HTL film exhibited the smoothest morphology (root-mean-square = 1.84 nm), whereas the pristine HTM film possessed a root-mean-square of 4.52 nm. Moreover, the incorporation of the POM@IL complex has raised the water contact angle of the HTL film from 71.3° to 83.5°.

Based on our previous works, we have validated that POMs clusters possess the capacity of oxidizing Spiro-OMeTAD under inert conditions without bringing damage to HTL or PSCs caused by exposure to air [40,41]. It is shown in the electron paramagnetic resonance (EPR) spectra of Spiro-OMeTAD solutions without and with POM, IL, POM@IL doping (Fig. 3a). Compared to the pure

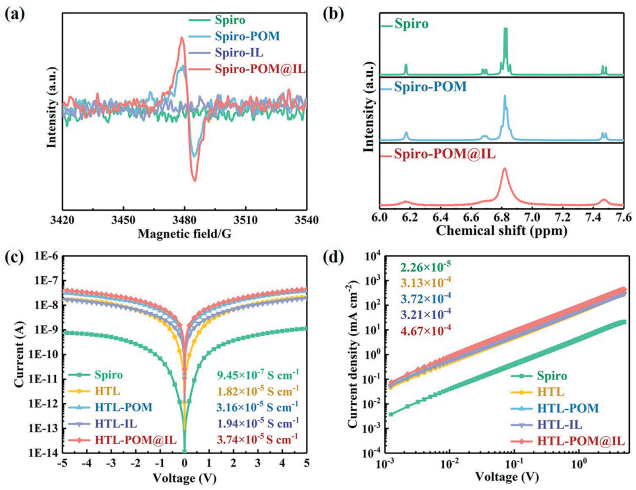

Fig. 3. (a) The EPR spectra of Spiro-OMeTAD solution and Spiro-OMeTAD solutions mixed with POM, IL, and POM@IL in chlorobenzene. (b) ^{1}H NMR spectra of Spiro-OMeTAD and Spiro-OMeTAD mixed with POM and POM@IL in DMSO-d6. (c) Current-voltage plots and (d) double logarithmic *J-V* curves based on different hole-only devices.

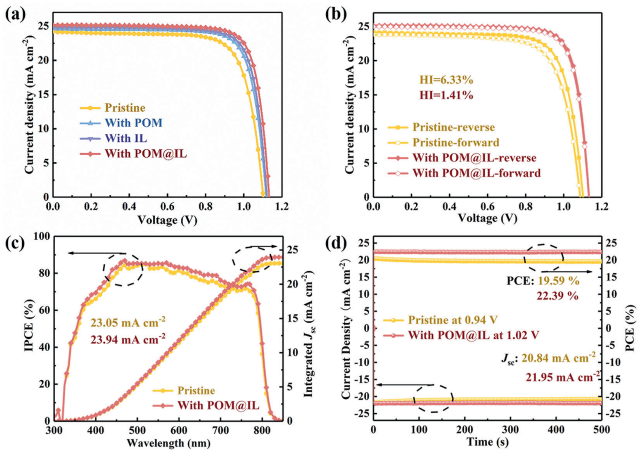

Fig. 4. (a) *J-V* curves of the champion pristine device and devices modified with POM, IL, and POM@IL. (b) *J-V* curves in different scan directions of the pristine device and device modified with POM@IL. (c) IPCE curves and the corresponding integrated J_{sc} of pristine PSCs and PSCs modified with POM@IL. (d) Steady-state PCEs and corresponding integrated current densities of the devices with and without POM@IL modification.

Spiro-OMeTAD solution and IL-doped Spiro-OMeTAD solution, the POMs cluster and POM@IL complex doped Spiro-OMeTAD solutions exhibited strong radical signals around 3480 G, which indicated the production of Spiro-OMeTAD$^{\bullet+}$ radical species. The electrostatic attractions between the POMs cluster and IL promoted the dispersion of the POMs cluster, which yielded more free radicals than the pure POMs cluster doped Spiro-OMeTAD solution. The ^{1}H NMR spectra based on different Spiro-OMeTAD solutions in DMSO-d6 (Fig. 3b) also proved the above conclusions. When mixing Spiro-OMeTAD with POMs and POM@IL complex, the proton signals around δ_H 6.8 ppm showed up-field shifts as well as significant decreases in intensities, which could be ascribed to the radical productions and change of chemical environments. The gradual decrease of proton signals indicated the increment of radical concentrations, which was in accordance with the EPR results.

To quantitively study the effects of POMs, IL, and POM@IL complex on the electrical properties of HTL (Supporting information), we have calculated the conductivities and hole mobilities based on different devices with and without doping (Figs. 3c and d). The device based on pure Spiro-OMeTAD exhibited an inferior conductivity of 9.45×10^{-7} S/cm and low hole mobility of 2.26×10^{-5} cm^2 V^{-1} s^{-1}. With the addition of Li-TFSI and TBP as dopants, the conductivity and mobility of the device were increased to 1.82×10^{-5} S/cm and 3.13×10^{-4} cm^2 V^{-1} s^{-1}, respectively (both aged in dry air). After further incorporation of POMs and POM@IL complex as additives (without aging in the air), the conductivities of the devices were raised to 3.16×10^{-5} S/cm and 3.74×10^{-5} S/cm, respectively. The addition of POMs clusters promoted the hole mobility to 3.72×10^{-4} cm^2 V^{-1} s^{-1}, and the device incorporated with POM@IL complex exhibited a superior hole mobility of 4.67×10^{-4} cm^2 V^{-1} s^{-1} (both aged under inert condition). Moreover, the hydrazine and carbonyl functional groups from IL were found to be able to passivate the defects and reduce the non-radiative recombination loss across the interface (Fig. S4 and Supplementary Note 4 in Supporting information). The calculated trap density for the devices was decreased from 1.36×10^{16} cm^{-3} (pristine device) to 8.76×10^{15} cm^{-3} (POM@IL-modified device).

We have fabricated a series of PSCs based on the different HTLs with the planar n-i-p configuration of FTO/TiO_2/perovskite/HTL. Based on the results obtained from the *J-V* curves (under AM 1.5G illumination at 100 mW/cm^2), we have plotted the statistical distribution box diagrams of photovoltaic parameters (PCE, V_{oc}, *FF*, and J_{sc}) for each group in Fig. S5 (Supporting information). The average PCEs of the devices were enhanced from 19.30% (pristine device) to 21.04% (POMs-doped device), 20.51% (IL-doped device), and 21.66% (POM@IL-doped device), respectively.

The *J-V* curves of the champion devices without and with different dopants as well as the summarized photovoltaic parameters were shown in Fig. 4a and Table S1 (Supporting information). The champion POM@IL-doped device exhibited an optimal PCE of 22.73%, J_{sc} of 25.15 mA/cm^2, V_{oc} of 1.133 V, and *FF* of 79.78%, exceeding that of the pristine device (PCE = 20.21%, J_{sc} = 24.20 mA/cm^2, V_{oc} = 1.103 V and *FF* = 75.72%). The effect of the POM@IL complex on the hysteresis behavior of PSCs was also investigated in Fig. 4b. The hysteresis index (HI) for each group was calculated according to the formula: HI = ($PCE_{reverse}$ - $PCE_{forward}$)/$PCE_{reverse}$. Due to the suppressed non-radiative recombination loss across the interface, the HI of the device was reduced from 6.33% to 1.41%.

Moreover, the photoelectrical responses of the pristine device and POM@IL-doped device ranged from 300 nm to 850 nm and were collected from the incident photon-to-electron conversion efficiency (IPCE) spectra in Fig. 4c. The incorporation of POM@IL complex facilitated an overall improvement in the photoelectrical response within the measured wavelength range. The integrated current densities of the pristine device and POM@IL-doped device were calculated to be 23.05 and 23.94 mA/cm^2, respectively. In addition, we have also held the pristine device and POM@IL-doped device at their maximum power points (MPP) and measured their steady-state power outputs (SPOs) in Fig. 4d. It was found that after holding at the MPP for 500 s under the continuous AM 1.5 G illumination, the POM@IL-doped device exhibited a stabilized SPO of 22.39% and a stabilized J_{sc} of 21.95 mA/cm^2. However, the pristine device exhibited a gradually decreasing SPO as well as J_{sc} at its MPP and under illumination. The addition of the POM@IL complex enhanced the light stability of PSCs and facilitated a steady charge transfer within the perovskite/HTL interface during the working function.

Additionally, we have also investigated the effects of the POM@IL complex on the stabilities of HTL films and PSCs. As shown in Figs. 5a and b, the pristine HTL film and POM@IL-modified HTL film were both aged at high humidity (25 °C, >90% RH) for 12 h. The POM@IL-modified HTL film didn't show evi-

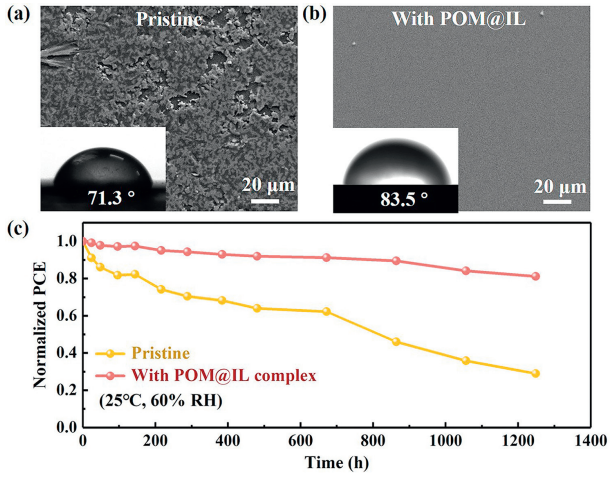

Fig. 5. (a, b) SEM images of pristine HTL film and HTL film modified with POM@IL after high humidity test. (c) Normalized PCEs of the PSCs with and without POM@IL modification under high humidity (25 °C, 60% RH).

dent degradation after the high humidity test, whereas the pristine HTL film completely degraded and affected the adjacent perovskite layer. By tracking the performances of the pristine device and POM@IL-modified device for over 1200 h in a high humidity environment (25 °C, 60% RH) in Fig. 5c, we found that the POM@IL-modified device showed significantly enhanced stability against humidity. After storing over 1200 h, the modified device retained 81.2% of its initial PCE, whereas the pristine device only retained 29.0% of its initial PCE. In summary, a POM@IL complex has been synthesized through a facile co-precipitate method to simultaneously enhance the performance and stability of PSCs. The electrostatic attraction between POMs and IL promoted the stabilization of Li-TFSI, which contributed to the finest morphology and excellent hydrophobicity. Through the synergistic oxidation strategy of POM@IL and Li-TFSI, the electrical properties of HTL were significantly enhanced under an inert condition without bringing harm to the HTL or PSCs. As a result, the POM@IL-modified device exhibited the optimal PCE of 22.73% and a superior V_{oc} of 1.133 V. In addition, the POM@IL complex-modified device retained a remarkable 81.2% of its initial PCE after storing under high humidity conditions (25 °C, 60% RH) for 1200 h. This work has validated the feasibility of the design and construction of POMs-based complexes with peculiar structures for the modification of photovoltaic devices and further encourages the investigation of other POMs derivatives for the construction of high-performance PSCs.

Declaration of competing interest

The authors declare that they have no known competing financial interests or personal relationships that could have appeared to influence the work reported in this paper.

Acknowledgments

This work is supported by the National Natural Science Foundation of China (Nos. 22072034 and 22001050), the China Postdoctoral Science Foundation (Nos. 2020T130147, 2020M681084, and 2022M710949), and the Postdoctoral Foundation of Heilongjiang Province (Nos. LBH-Z19059, and LBH-Z22106) the Natural Science Foundation of Heilongjiang Youth Fund (No. YQ2021B002).

Supplementary materials

Supplementary material associated with this article can be found, in the online version, at doi:10.1016/j.cclet.2023.108933.

References

[1] Best research-cell efficiency chart, 2023, https://www.nrel.gov/pv/cell-efficiency.html, accessed 29 January 2023.
[2] S. Zhan, W. Din, Z. S, et al., Adv. Powder Mater. 1 (2022) 100036.
[3] Z. Li, M. Wu, L. Yang, et al., Adv. Funct. Mater. 33 (2023) 2212606.
[4] N. Li, A. Feng, X. Guo, et al., Adv. Energy Mater. 12 (2022) 2103241.
[5] X. Guo, N. Li, Y. Xu, et al., Adv. Funct. Mater. 33 (2023) 2213995.
[6] T. Webb, X. Liu, J.E.W. Robert, et al., Adv. Energy Mater. 12 (2022) 2200666.
[7] T. Zhang, F. Wang, H.B. Kim, et al., Science 377 (2022) 495–501.
[8] P. Yan, D. Yang, H. Wang, et al., Energy Environ. Sci. 15 (2022) 3630–3669.
[9] B. Tan, S.R. Raga, A.S.R. Chesman, et al., Adv. Energy Mater. 9 (2019) 1901519.
[10] Y. Liu, Z. Hong, Q. Chen, Adv. Mater. 28 (2016) 440–446.
[11] L. Caliò, M. Salado, S. Kazim, et al., Joule 2 (2018) 1800–1815.
[12] F.M. Rombach, S.A. Haque, T.J. Macdonald, Energy Environ. Sci. 14 (2021) 5161–5190.
[13] C.M. Wolff, P. Caprioglio, M. Stolterfoht, et al., Adv. Mater. 31 (2019) 1902762.
[14] I. Gelmetti, N. Montcada, A. Pérez-Rodríguez, et al., Energy Environ. Sci. 12 (2019) 1309–1316.
[15] T. Kirchartz, Philos. Trans. R. Soc. A 377 (2019) 20180286.
[16] A. Abate, T. Leijtens, S. Pathak, et al., Phys. Chem. Chem. Phys. 15 (2013) 2572.
[17] H.J. Snaith, M. Grätzel, Appl. Phys. Lett. 89 (2006) 262114.
[18] U.B. Cappel, T. Daeneke, U. Bach, Nano Lett. 12 (2012) 4925–4931.
[19] R.L. Forward, K.Y. Chen, D.M. Weekes, et al., ACS Energy Lett. 4 (2019) 2547–2551.
[20] Z. Li, C. Xiao, Y. Yang, et al., Energy Environ. Sci. 10 (2017) 1234–1242.
[21] F. Lin, J. Luo, Y. Zhang, et al., J. Mater. Chem. A 11 (2023) 2544–2567.
[22] Y. Liu, T. Liu, X. Guo, et al., Adv. Funct. Mater. 33 (2023) 2210028.
[23] Q. Lou, G. Lou, H. Guo, et al., Adv. Energy Mater. 12 (2022) 2201344.
[24] J. Xia, Y. Zhang, C. Xiao, et al., Joule 6 (2022) 1689–1709.
[25] Y. Han, G. Zhang, H. Xie, et al., Nano Energy 96 (2022) 107072.
[26] D.L. Long, E. Burkholder, L. Cronin, Chem. Soc. Rev. 36 (2007) 105.
[27] M.R. Horn, A. Singh, S. Alomari, et al., Energy Environ. Sci. 14 (2021) 1652–1700.
[28] J. Duan, H. Shabbir, Z. Chen, et al., J. Am. Chem. Soc. 145 (2023) 7268–7277.
[29] L. Liu, Z. Wu, Z. Zheng, et al., Chin. Chem. Lett. 33 (2022) 4326–4330.
[30] A.V. Anyushin, A. Kondinski, T.N. Parac-Vogt, Chem. Soc. Rev. 49 (2020) 382–432.
[31] N.I. Gumerova, A. Rompel, Nat. Rev. Chem. 2 (2018) 0112.
[32] Q. Wang, B. Xu, Y. Wang, et al., Inorg. Chem. 60 (2021) 7753–7761.
[33] M. Martin-Sabi, J. Soriano-López, R.S. Winter, et al., Nat. Catal. 1 (2018) 208–213.
[34] Q. Kang, Q. Liao, C. Yang, et al., Adv. Energy Mater. 12 (2022) 2103892.
[35] A. Misra, I.F. Castillo, D. P, et al., Angew. Chem. Int. Ed. 57 (2018) 14926–14931.
[36] S. Herrmann, L.D. Matteis, J.M. Fuente, et al., Angew. Chem. Int. Ed. 56 (2017) 1667–1670.
[37] M. Zhang, A.M. Zhang, X.X. Wang, et al., J. Mater. Chem. A 6 (2018) 8735–8741.
[38] J. Meng, M. Lei, C. Lai, et al., Angew. Chem. Int. Ed. 60 (2021) 23256–23266.
[39] J. Meng, F. Chu, J. Hu, et al., Adv. Funct. Mater. 29 (2019) 1902220.
[40] B. Hu, J. Zhang, Y. Yang, et al., ACS Appl. Mater. Interfaces 14 (2022) 17610–17620.
[41] F. Wu, S. Mabrouk, M. Han, et al., J. Energy Chem. 76 (2023) 414–420.